PHYSICAL REVIEW B **110**, 014207 (2024)

Editors' Suggestion

Effects of nonlocal pseudopotentials on the electrical and thermal transport properties of aluminum: A density functional theory study

Qianrui Liu (刘千锐)
HEDPS, CAPT, College of Engineering and School of Physics, Peking University, Beijing 100871, People's Republic of China

Mohan Chen (陈默涵)*
HEDPS, CAPT, College of Engineering and School of Physics, Peking University, Beijing 100871, People's Republic of China
and AI for Science Institute, Beijing 100080, People's Republic of China

(Received 26 February 2024; revised 9 June 2024; accepted 25 June 2024; published 22 July 2024)

Accurate prediction of electron transport coefficients is crucial for understanding warm dense matter. Utilizing density functional theory (DFT) with the Kubo-Greenwood formula is widely used to evaluate the electrical and thermal conductivities of electrons. By adding the nonlocal potential correction term that appears in the dynamic Onsager coefficient and using two different norm-conserving pseudopotentials, we predict the electrical and thermal conductivities of electrons for liquid Al (1000 K) and warm dense Al (0.2 to 10 eV). We systematically investigate the effects of nonlocal terms in the pseudopotentials and the frozen-core approximation on the conductivities. We find that taking into account the nonlocal potential correction and validating the frozen core approximation is essential for accurately calculating the electrical and thermal transport properties of electrons across a wide range of temperatures.

DOI: 10.1103/PhysRevB.110.014207

I. INTRODUCTION

Warm dense matter (WDM) is a state of matter characterized by extremely high temperature, high density, and high pressure that commonly exists and plays a significant role in the interiors of giant planets [1,2] and inertial confinement fusion [3]. Consequently, research on WDM has emerged as one of the most prominent areas in high-energy density physics. Nonetheless, generating and analyzing WDM in laboratory settings presents a significant challenge, making computational modeling an indispensable tool for understanding this unique state of matter. Furthermore, given that WDM comprises partially ionized electrons and strongly coupled ions, incorporating quantum mechanics is essential for accurately simulating and investigating its properties. Nevertheless, even with the use of modern high-performance computing, it is still challenging to simulate the structural, dynamical, and transport properties of WDM at extremely high temperatures [4,5].

In recent years, various first-principles methods, such as the Kohn-Sham density functional theory (KSDFT) [6–8], the orbital-free density functional theory (OFDFT) [9,10], and the path integral Monte Carlo [11–13], have been developed to investigate WDM across a wide range of temperatures and pressures [14–24]. Additionally, several KSDFT-based methods have been proposed to overcome the challenge of simulating WDM, including the extended first-principles molecular dynamics [25–28], the stochastic DFT [29,30], and the mixed deterministic-stochastic DFT [31–33], etc. Within the framework of DFT, the exchange-correlation (XC) functionals considering temperature effects have been developed [34,35] to yield more accurate results for the matter under extreme conditions. In addition, machine-learning-based molecular dynamics [36,37], known for their ability to efficiently simulate large systems while retaining high accuracy, have recently been widely utilized to investigate WDM with larger systems or longer trajectories [23,24,33,38–41].

Several methods have been developed to describe the ion-electron interactions within the framework of DFT. First, adopting norm-conserving pseudopotentials (NCPPs) [42] in DFT calculations provides an accurate yet efficient way to describe the behavior of valence electrons while neglecting the fast-varying, highly localized core electron wavefunctions. Among the NCPPs, the Kleinman-Bylander (KB) approach [43] employs a single local radial potential and a few separable l-dependent nonlocal projectors. Recently, Hamann [44,45] has developed optimized norm-conserving Vanderbilt (ONCV) pseudopotentials with two projectors, which enhances the accuracy and lower cutoff energies when compared to the traditional NCPPs [46,47]. Second, the ultrasoft pseudopotentials (USPPs) [48] remove the norm-conserving condition and provide a smoother potential to describe the electron-ion interaction, allowing for a lower-energy cutoff and thus reducing computational costs. Third, another notable approach is the projector augmented-wave (PAW) method [49], which allows recovery of all-electron quantities while still benefiting from reduced computational costs compared to the all-electron methods. Although the USPPs and PAW methods can reduce the energy cutoff and improve efficiency, they come with additional complexity in the implementation of certain calculations, such as density-functional perturbation theory (DFPT) [50]. On the other hand, NCPPs remain widely used due to their simplicity and ease of implementation. In this paper, we adopt the NCPPs.

---

*Contact author: mohanchen@pku.edu.cn

The electrical and thermal transport properties are essential in fields such as laser heating [51], hydrodynamic instability [52], and metal-nonmetal transitions [53]. Both electrons and ions contribute to the electrical and thermal transport, but the former becomes more important in WDM, as shown in Ref. [24] (over 200 times higher than the latter). In addition, nonadiabatic electron-ion coupling and the consideration of nonequilibrium states of ions [54,55] may also affect the results, but this is not the focus of this paper. In this regard, we focus on calculating the electrical and thermal conductivities driven by electrons in the equilibrium state. To do this, KSDFT-based molecular dynamics and the Kubo-Greenwood (KG) method are employed, which have been successfully applied to various systems, including liquid metals [56], silica [57], and plastics [58], etc. In particular, various studies have adopted this method to study transport properties of WDM and obtained valuable results [20–22,24].

Notably, when employing the KG formula, the presence of nonlocal potentials in NCPPs leads to a correction term in this formula (*vide infra*). Unfortunately, some previous studies have overlooked the influences of these corrections on the computed properties [24,59,60]. To the best of our knowledge, when the NCPPs are employed to study the conductivities of WDM, the effects of nonlocal potential corrections that appear in the Kubo-Greenwood formula are still inconclusive. In this regard, we have implemented the nonlocal potential corrections with the plane wave basis sets and under periodic boundary conditions in the ABACUS package [32,61,62]. Next, we select Al at two densities (2.35 and 2.70 g/cm3) and the temperature range 0.086–10 eV. We first compute the electrical and thermal conductivities of electrons for aluminum (Al) with the revised formula. Next, we thoroughly investigate the effects of using two different pseudopotentials with or without the nonlocal potential corrections on the computed conductivities. Finally, we analyze the density of states, the decomposed electrical conductivity, and the Lorenz number of Al across a wide range of temperatures and elucidate our findings.

The paper is organized as follows. In Sec. II, we provide a brief introduction to the Kubo-Greenwood formula and explain the formulas to implement the nonlocal potential corrections with the plane wave basis set. Additionally, we outline the setup for calculating the electrical and thermal conductivities of Al. In Sec. III, we present our results and analysis for Al. The concluding remarks are shown in Sec. IV.

II. METHODS

A. Electrical conductivity and thermal conductivity

To calculate the electrical and thermal conductivities, we first need to compute the dynamic Onsager coefficients $L_{mn}(\omega)$ $(m,n=1,2)$ using the Kubo-Greenwood formula. The equation is as follows:

$$L_{mn}(\omega)=(-1)^{m+n}\frac{2\pi e^2}{3\omega\Omega}\times\sum_{ij\alpha\mathbf{k}}W(\mathbf{k})\left(\frac{\epsilon_{i\mathbf{k}}+\epsilon_{j\mathbf{k}}}{2}-\mu\right)^{m+n-2}|\langle\Psi_{i\mathbf{k}}|\hat{v}_\alpha|\Psi_{j\mathbf{k}}\rangle|^2\times[f(\epsilon_{i\mathbf{k}})-f(\epsilon_{j\mathbf{k}})]\delta(\epsilon_{j\mathbf{k}}-\epsilon_{i\mathbf{k}}-\hbar\omega),\tag{1}$$

where ω represents the frequency, e is the elementary charge, Ω denotes the volume of the cell, and μ refers to the chemical potential. $\Psi_{i\mathbf{k}}$ represents the wave function of the ith band with $\mathbf{k}$ being a point in the first Brillouin zone, and the corresponding eigenvalue is $\epsilon_{i\mathbf{k}}$. $W(\mathbf{k})$ represents the weight of k points and $\hat{v}_\alpha$ denotes the αth component of the velocity operator $\hat{\mathbf{v}}$. The Fermi-Dirac distribution function of electrons is f, and δ is the delta function. In practice, the delta function is approximated by a Gaussian function,

$$\delta(E)\approx\frac{1}{\sqrt{2\pi}\Delta E}\exp(-E^2/(2\Delta E^2)),\tag{2}$$

where ΔE determines the width of the Gaussian function. In this paper, we set the full width at half maximum (FWHM $=2.3548\Delta E$) to 0.1 eV.

With the above formulas, the electrical conductivity σ and thermal conductivity κ of electrons respectively take the form of

$$\sigma=\lim_{\omega\to 0}L_{11}(\omega),\tag{3}$$

$$\kappa=\lim_{\omega\to 0}\frac{1}{e^2T}\left(L_{22}(\omega)-\frac{L_{12}^2(\omega)}{L_{11}(\omega)}\right).\tag{4}$$

In addition, to allow for extrapolation to zero frequency, we employ specific functions to fit the frequency-dependent lines, which can be found within the Supplemental Material (SM) [63]. It is worth noting that the choices of different fitting functions do not substantially affect the results when the fitting range is close to the zero frequency $\omega=0$.

B. Nonlocal potential correction

The velocity operator [64] in quantum mechanics, denoted as $\hat{\mathbf{v}}$, is defined as

$$\hat{\mathbf{v}}=\frac{i}{\hbar}[\hat{H},\hat{\mathbf{r}}].\tag{5}$$

Here, $\hat{H}$ represents the Hamiltonian operator, and $\hat{\mathbf{r}}$ represents the position operator. For Hamiltonian that contains the nonlocal pseudopotential, an additional commutator enters the formalism as [64,65]

$$\hat{\mathbf{v}}=\frac{\hat{\mathbf{p}}}{m_e}+\frac{i}{\hbar}[\hat{V}_{\mathrm{NL}},\hat{\mathbf{r}}],\tag{6}$$

where $\hat{\mathbf{p}}$ is the momentum operator, m_e is the mass of electrons, and $\hat{V}_{\mathrm{NL}}$ depicts the nonlocal pseudopotential operator. When dealing with the Hamiltonian that only contains the local potential terms, the velocity operator can be represented by the momentum operator alone. However, for systems with nonlocal potential terms, the correction term in the second part of Eq. (6) cannot be ignored.

In this paper, we adopt the plane-wave basis set with the periodic boundary conditions and the k-point sampling method [66], with which the electronic wave function can be written as

$$|\Psi_{i\mathbf{k}}\rangle=\sum_{\mathbf{G}}c_{i\mathbf{k}}(\mathbf{G})|\mathbf{k}+\mathbf{G}\rangle,\tag{7}$$

where $\mathbf{G}$ depicts the plane wave basis and $\{c_{i\mathbf{k}}\}$ are the coefficients of plane wave basis sets for band i. We denote the wave vector as $\mathbf{q} = \mathbf{k} + \mathbf{G}$, which satisfies $\sum_{\mathbf{q}} |\mathbf{q}\rangle\langle\mathbf{q}| = I$ with I being an identity matrix. $c_{i\mathbf{k}}(\mathbf{G})$ takes the formula of

$$c_{i\mathbf{k}}(\mathbf{G}) = \langle\mathbf{q}|\Psi_{i\mathbf{k}}\rangle = \Psi_{i\mathbf{k}}(\mathbf{q}). \tag{8}$$

Thus, the nonlocal correction term in the velocity matrix has the form of

$$\begin{aligned}\langle\Psi_{i\mathbf{k}}|[\hat{V}_{\mathrm{NL}}, \hat{\mathbf{r}}]|\Psi_{j\mathbf{k}}\rangle &= \sum_{\mathbf{q}\mathbf{q}'} \langle\Psi_{i\mathbf{k}}|\mathbf{q}\rangle\langle\mathbf{q}|[\hat{V}_{\mathrm{NL}}, \hat{\mathbf{r}}]|\mathbf{q}'\rangle\langle\mathbf{q}'|\Psi_{j\mathbf{k}}\rangle, \\ &= \sum_{\mathbf{q}\mathbf{q}'} \Psi^*_{i\mathbf{k}}(\mathbf{q})\langle\mathbf{q}|[\hat{V}_{\mathrm{NL}}, \hat{\mathbf{r}}]|\mathbf{q}'\rangle\Psi_{j\mathbf{k}}(\mathbf{q}'). \end{aligned} \tag{9}$$

Since the position operator $\hat{\mathbf{r}}$ is ill-defined in a periodic system, the $[\hat{V}_{\mathrm{NL}}, \hat{\mathbf{r}}]$ operator can be calculated in the reciprocal space [67] as

$$\langle\mathbf{q}|[\hat{V}_{\mathrm{NL}}, \hat{\mathbf{r}}]|\mathbf{q}'\rangle = (\nabla_{\mathbf{q}} + \nabla_{\mathbf{q}'})V_{\mathrm{NL}}(\mathbf{q}, \mathbf{q}'). \tag{10}$$

To compute the above term, we need to first calculate the nonlocal pseudopotential term in the plane wave basis, which is

$$V_{\mathrm{NL}}(\mathbf{q}, \mathbf{q}') = \sum_{\kappa=1}^{N_{\mathrm{t}}} S^{\kappa}(\mathbf{q}' - \mathbf{q})V^{\kappa}_{\mathrm{NL}}(\mathbf{q}, \mathbf{q}'), \tag{11}$$

where N_{t} is the number of atom types, $V^{\kappa}_{\mathrm{NL}}(\mathbf{q}, \mathbf{q}')$ is the nonlocal pseudopotential of the κth element, and the first part S^{κ} is the structure factor of the κth element, given by

$$S^{\kappa}(\mathbf{G}) = \sum_{j=1}^{N_{\kappa}} \exp(i\mathbf{G}\cdot\tau_{\kappa j}), \tag{12}$$

where N_{κ} denotes the number of κ-type atoms and τ represents the position of the atom. In this case, we find

$$(\nabla_{\mathbf{q}} + \nabla_{\mathbf{q}'})S^{\kappa}(\mathbf{q}' - \mathbf{q}) = 0. \tag{13}$$

Furthermore, the second part is the nonlocal potential for the κth element and can be calculated using the formula of

$$V^{\kappa}_{\mathrm{NL}}(\mathbf{q}, \mathbf{q}') = \sum_{ll'mm'} D^{\kappa}_{lm,l'm'}\beta^{\kappa}_{lm}(\mathbf{q})\beta^{\kappa *}_{l'm'}(\mathbf{q}'), \tag{14}$$

where $\beta^{\kappa}_{lm}(\mathbf{q})$ is the nonlocal projector of NCPPs expanded with the plane wave basis. Additionally, the atom type is κ and the coefficient matrix of projectors is $D^{\kappa}_{lm,l'm'}$. In detail, $\beta^{\kappa}_{lm}(\mathbf{q})$ is written as

$$\beta^{\kappa}_{lm}(\mathbf{q}) = \frac{4\pi(-i)^l}{\sqrt{\Omega}} f^{\kappa}_l(q)Y_{lm}(\hat{\mathbf{q}}). \tag{15}$$

Here, the radial part is obtained by

$$f^{\kappa}_l(q) = \int_0^{+\infty} F^{\kappa}_l(r)j_l(qr)r^2\mathrm{d}r. \tag{16}$$

In this equation, $rF^{\kappa}_l(r)$ is a one-dimensional nonlocal projector read from the pseudopotential file, j_l depicts the spherical Bessel function, and $Y_{lm}(\hat{\mathbf{q}})$ is the spherical harmonic function.

Based on the above formulas, the key part of the nonlocal potential correction term can be expressed as

$$\begin{aligned}&(\nabla_{\mathbf{q}} + \nabla_{\mathbf{q}'})V_{\mathrm{NL}}(\mathbf{q}, \mathbf{q}') \\ &= \sum_{\kappa=1}^{N_{\mathrm{t}}} S^{\kappa}(\mathbf{q}' - \mathbf{q})(\nabla_{\mathbf{q}} + \nabla_{\mathbf{q}'})V^{\kappa}_{\mathrm{NL}}(\mathbf{q}, \mathbf{q}') \\ &= \sum_{\kappa=1}^{N_{\mathrm{t}}} S^{\kappa}(\mathbf{q}' - \mathbf{q}) \sum_{ll'mm'} D^{\kappa}_{lm,l'm'} \\ &\quad \times \left[\mathbf{g}^{\kappa}_{lm}(\mathbf{q})\beta^{\kappa *}_{l'm'}(\mathbf{q}') + \beta^{\kappa}_{lm}(\mathbf{q})\mathbf{g}^{\kappa *}_{l'm'}(\mathbf{q}')\right],\end{aligned} \tag{17}$$

where $\mathbf{g}^{\kappa}_{lm}(\mathbf{q})$ represents the gradient of $\beta^{\kappa}_{lm}(\mathbf{q})$ with respect to $\mathbf{q}$ and has the following form:

$$\begin{aligned}\mathbf{g}^{\kappa}_{lm}(\mathbf{q}) &= \frac{4\pi(-i)^l}{\sqrt{\Omega}} \\ &\quad \times \left[q^l Y_{lm}(\hat{\mathbf{q}})\nabla_{\mathbf{q}}\left(\frac{f^{\kappa}_l(q)}{q^l}\right) + \frac{f^{\kappa}_l(q)}{q^l}\nabla_{\mathbf{q}}(q^l Y_{lm}(\hat{\mathbf{q}}))\right].\end{aligned} \tag{18}$$

It should be noted that the gradient of $q^l Y_{lm}(\hat{\mathbf{q}})$ is used instead of the gradient of $Y_{lm}(\hat{\mathbf{q}})$ to avoid the singularity at $\mathbf{q} = \mathbf{0}$.

In total, the velocity matrix $\langle\Psi_{i\mathbf{k}}|\hat{v}_{\alpha}|\Psi_{j\mathbf{k}}\rangle$ in Eq. (1), can be evaluated in the reciprocal space with plane wave basis as

$$\sum_{\mathbf{q}\mathbf{q}'} \Psi^*_{i\mathbf{k}}(\mathbf{q})\left(\frac{\hbar\mathbf{q}}{m_e}\delta(\mathbf{q} - \mathbf{q}') + \frac{i}{\hbar}\langle\mathbf{q}|[\hat{V}_{\mathrm{NL}}, \mathbf{r}]|\mathbf{q}'\rangle\right)\Psi_{j\mathbf{k}}(\mathbf{q}'), \tag{19}$$

where the second term is calculated through Eqs. (10) and (17).

C. Computational details

With the above formulas implemented, we performed a systematic study on the electrical and thermal conductivities of Al at a temperature range 0.2–10 eV. The densities were chosen to be 2.35 and 2.70 g/cm^3. First, to obtain atomic configurations of Al at various temperatures, we utilized Born-Oppenheimer molecular dynamics (BOMD) simulations based on OFDFT. The Wang-Teter (WT) kinetic energy density functional [68] was employed and has been validated in previous studies [23,24]. During BOMD simulations, the Nosé-Hoover thermostat [69,70] was adopted in the NVT ensemble. We utilized 256 atoms in a cell for temperatures up to 5 eV. For higher temperatures, we used 108 atoms. The energy cutoff for the electron density was set to 80 Ry. The simulations were performed for 4000 steps with time steps being $\frac{r_s}{60\bar{v}}$, where r_s was the Weigner-Setz radius and $\bar{v} = \sqrt{T/m}$ was the average velocity of atoms. Here, T is the temperature and m is the mass of an Al atom. From the BOMD trajectories, we selected five atomic configurations to calculate the electrical and thermal conductivities of electrons in the Al system, which has been tested to be converged (see the SM [63]).

Second, we employed the Kohn-Sham density functional theory (KSDFT) and the Kubo-Greenwood formula, as shown in Eqs. (1), (3), and (4), to calculate the Onsager coefficients and subsequently the electrical and thermal conductivities of Al. We used an energy cutoff of 50 Ry to describe the wave functions in KSDFT calculations. In particular, we utilized two NCPPs, which are named NC11 (11 valence electrons) and NC3 (three valence electrons). On the one hand, the NC11 pseudopotential, generated using the optimized norm-conserving Vanderbilt pseudopotential method via the ONCVPSP package [44,45], had 11 valence electrons and a cutoff radius of 0.50 Å. On the other hand, the NC3 pseudopotential was generated through the PSlibrary package [71] using the Troullier-Martins method [72]. In addition, the NC3 pseudopotential contained three valence electrons, and the cutoff radius was set to 1.38 Å. To ensure convergence, we selected a larger number of KS bands at higher temperatures, ensuring that the occupation of the last band was smaller than 1e-5. For temperatures of 1000 K and 0.2 eV, we used a $5 \times 5 \times 5$ k-point and $3 \times 3 \times 3$ k-point mesh [66], respectively. For temperature range 0.5–1.0 eV, we employed a $2 \times 2 \times 2$ k-point mesh, and we only considered the Γ point at higher temperatures.

Finally, both OFDFT and KSDFT simulations employed the Perdew-Burke-Ernzerhof (PBE) [73] XC functional. A previous paper [24] had demonstrated that using either PBE or LDA [7] XC did not significantly affect the results. Additionally, we also tested a temperature-dependent XC functional called KSDT [34,35] and found that it did not substantially influence the results within the temperature and density range studied in this paper (see the SM [63]). All of the above simulations were performed using the ABACUS v3.2 package [61,74].

III. RESULTS AND DISCUSSION

A. Liquid Al

Figures 1(a) and 1(b) respectively illustrate the calculated frequency-dependent electrical and thermal conductivities of liquid Al with and without the nonlocal pseudopotential corrections. In addition, first-principles data from previous studies [56,75] and experimental results are displayed for comparison. All of the above data are obtained for liquid Al at 1000 K with a density of 2.35 g/cm^3. Our calculations utilize a simulation cell containing 256 atoms and a $5{\times}5 \times 5$ shifted k-point mesh to ensure convergence. We use the NC11 pseudopotential with 11 valence electrons for liquid Al. In particular, to extrapolate the frequency-dependent electrical and thermal conductivities to zero frequency and obtain the transport properties, we employ the Drude formula to fit the frequency-dependent (dynamic) electrical conductivity and use a linear function to fit the thermal conductivity. The fitting range is 0.15–1.00 eV. Note that the experimental data of Mills *et al.* [76] and Rhim *et al.* [77] are obtained by substituting 1000 K into the corresponding fitting equation, while the results of Abdellah *et al.* [78] and Brandt *et al.* [79] are obtained by linearly interpolating their results from the table to 1000 K.

Notably, we find both zero-frequency electrical and thermal conductivities ($\omega = 0$) of Al obtained with the nonlocal potential correction (labeled as NC11 corr. fitting) yield substantially smaller values than the ones without the correction (labeled as NC11 fitting). In detail, the calculated electrical conductivity at $\omega = 0$ with the nonlocal potential correction shown in Fig. 1(a) is 3.89×10^6 Sm^{-1}, which is 40.1% lower than the value of 5.45×10^6 Sm^{-1} without correction. For comparison, the DC electrical conductivity ($\omega = 0$) measured by Abdellah *et al.* [78], Rhim *et al.* [77], and Brandt *et al.* [79] from experiments are 4.07×10^6, 3.99×10^6, and 4.05×10^6 Sm^{-1}, respectively. We conclude that the value with the nonlocal potential correction matches better with the experimental data. In Fig. 1(b), the thermal conductivity at $\omega = 0$ calculated with the nonlocal potential correction (labeled as NC11 corr. fitting) is 96 Wm^{-1}K^{-1}, which is 40.6% lower than the value of 135 Wm^{-1}K^{-1} without correction (labeled as NC11 fitting). On the other hand, experimental measurements by Mill *et al.* [76], Rhim *et al.* [77], and Brandt *et al.* [79] yield values of 103, 98, and 96 Wm^{-1}K^{-1}, respectively. Again, we find the calculated data with the nonlocal potential correction agrees well with the experimental results.

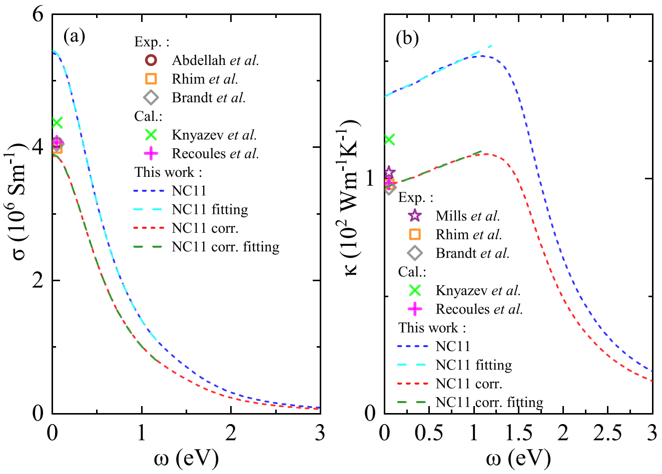

FIG. 1. (a) Frequency-dependent electrical (σ in 10^6 Sm^{-1}) and (b) thermal conductivities (κ in 10^2 Wm^{-1}K^{-1}) of liquid Al at $T =$ 1000 K. The NC11 label refers to a norm-conserving pseudopotential with 11 valence electrons. The corr. label depicts the line obtained by considering the nonlocal pseudopotential correction, while the fitting label depicts the line obtained by a fitting method. Here, the electrical conductivities are fitted with a Drude model, while the thermal conductivities are linearly fitted. Computational results from Recoules *et al.* [56] and Knyazev *et al.* [75], as well as available experimental data at $\omega = 0$ eV are shown for comparison [76–79].

We also compare the calculated results with previous computational works by Recoules *et al.* [56], and Knyazev *et al.* [75]. In detail, Knyazev *et al.* [75] used three valence electrons in a USPP to describe Al, and the nonlocal potential corrections are not included in the results. More discussions are in the later session. On the other hand, Recoules *et al.* [56] utilized the density functional perturbation theory (DFPT) to account for the effects of nonlocal potential in NCPPs and obtained better results compared to experimental results. The above results demonstrate the importance of considering the nonlocal potential correction in computed DC electrical and thermal conductivities for liquid Al.

B. Warm dense Al with a density of 2.35 g/cm^3

Besides the nonlocal potential correction, the use of frozen core approximation in pseudopotentials may substantially

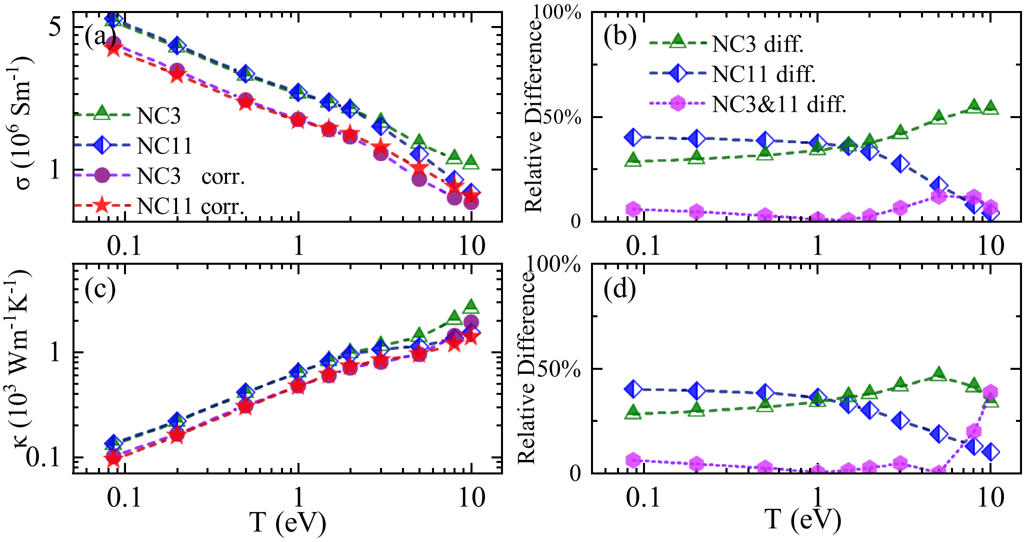

FIG. 2. (a) Electrical (σ in Sm^{-1}) and (c) thermal conductivities (κ in $10^3\,\mathrm{Wm}^{-1}\mathrm{K}^{-1}$) of liquid and warm dense Al at a density of $2.35\ \mathrm{g/cm}^3$ and a temperature range 0.086–10 eV. The simulation cell contains 256 atoms for temperatures no more than 5 eV and 108 atoms for higher temperatures. The NC3 and NC11 labels refer to two norm-conserving pseudopotentials with valence electrons being 3 and 11, respectively. The "corr." label depicts the data obtained by considering the nonlocal pseudopotential correction. (b) and (d) plot the relative differences of σ and κ, respectively. The label "NCx diff." represents the relative difference computed by the formula of $|V_{\mathrm{NCx}} - V_{\mathrm{NCx\ corr.}}|/V_{\mathrm{NCx\ corr.}}$, where x is 3 or 11 and V is σ or κ. Additionally, the term "NC3&11 diff." depicts $|V_{\mathrm{NC3\ corr.}} - V_{\mathrm{NC11\ corr.}}|/V_{\mathrm{NC11\ corr.}}$.

affect the computed electrical and thermal conductivities of Al. Figures 2(a) and 2(c) show the calculated electrical and thermal conductivities of Al in terms of using two different pseudopotentials, respectively. The temperature range is 0.086–10 eV. The two used NCPPs are named as the NC3 and NC11 pseudopotentials. Here, the NC3 and NC11 labels refer to two norm-conserving pseudopotentials with valence electrons being 3 and 11, respectively. In addition, we compute the electrical and thermal conductivities with and without the nonlocal pseudopotential corrections. We have the two following findings in Figs. 2(a) and 2(c).

Firstly, in the temperature range studied in Fig. 2(a), the computed electrical conductivity decreases as temperature increases, which can be explained by an increase in the collision frequency of electrons with elevated temperatures. Conversely, Fig. 2(c) illustrates the computed thermal conductivity becomes larger with rising temperatures. Secondly, comparing the data with and without nonlocal potential corrections reveals that the corrected values are systematically lower than those without corrections for both electrical and thermal conductivities.

Figures 2(b) and 2(d) further illustrate the relative differences for the calculated electrical and thermal conductivities, respectively. Interestingly, we find the nonlocal potential corrections for the NC3 pseudopotential exhibit a trend of becoming substantially larger at around 2 eV and higher temperatures. This can be explained by the fact that the NC3 pseudopotential has eight fewer electrons than the NC11 pseudopotential in the frozen core approximation; the missing eight electrons in the NC3 pseudopotential affect the computed conductivities at high temperatures, so the NC3 pseudopotential approximates the ion-electron interactions worse than the NC11 pseudopotential at high temperatures. Consequently, the nonlocal pseudopotential loses transferability and suffers more errors at higher temperatures.

In contrast, when the NC11 pseudopotential is used, we observe that the nonlocal potential corrections tend to exhibit another trend of becoming substantially smaller at around 2 eV and higher temperatures. Since the errors introduced by an insufficient number of electrons are minimized, we attribute this trend to the velocity operator shown in Eq. (6) comprising both the kinetic energy term and nonlocal potential term of electrons, with the former one becoming increasingly larger than the latter one as the temperature rises.

We also compare the relative differences of electrical and thermal conductivities obtained by the two different pseudopotentials, i.e., NC3 and NC11. At low temperatures below 2 eV, the two pseudopotentials yield similar results, but as the temperature rises over 2 eV, the differences become increasingly larger, indicating again that the invalidity of the frozen-core approximation for the NC3 pseudopotential at higher temperatures.

C. Warm dense Al with a density of 2.7 g/cm^3

Figures 3(a) and 3(c) illustrate the computed temperature-dependent electrical and thermal conductivities as obtained from the NC11 pseudopotential, respectively. The temperature ranges from 0.2 to 10 eV while the density of Al is chosen to be $\rho = 2.7\ \mathrm{g/cm}^3$. We also compute the electrical and thermal conductivities by using the NC3 pseudopotential. In addition, available experimental results are added for comparison. Although the trends exhibited by the conductivities at the density of $\rho = 2.7\ \mathrm{g/cm}^3$ are similar to those of $\rho = 2.35\ \mathrm{g/cm}^3$ shown in Fig. 2, there are some points worth noting.

We compare our calculated data in Fig. 3(a) with the experimental data reported by Milchberg *et al.* [81] and Sperling *et al.* [82]. Our calculated electrical conductivities (NC11 corr.) are larger than those from Sperling *et al.* [82]. Meanwhile, they align well with the data from Milchberg *et al.*

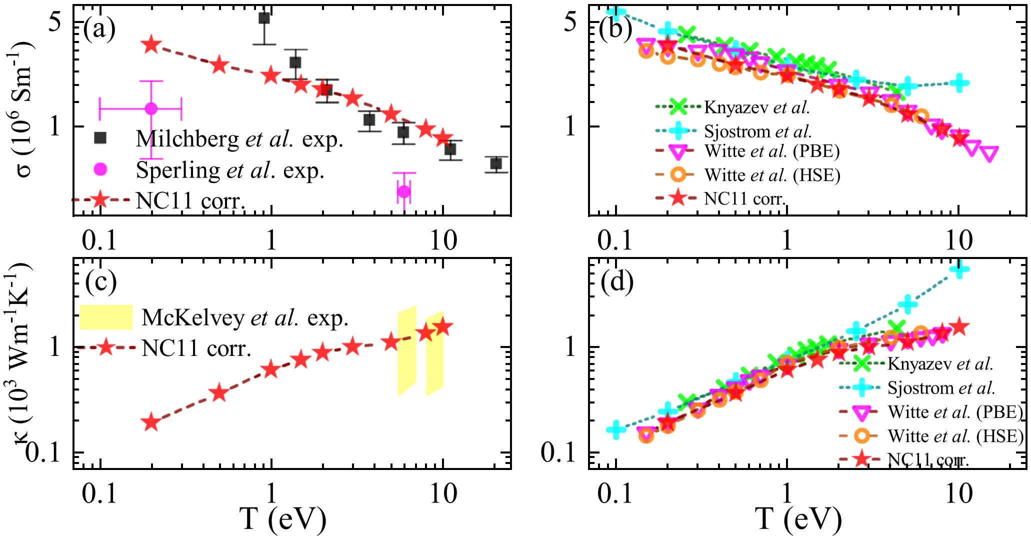

FIG. 3. [(a),(b)] Electrical (σ in 10^6 Sm^{-1}) and [(c),(d)] thermal conductivities (κ in 10^3 Wm^{-1}K^{-1}) of liquid and warm dense Al at a density of 2.70 g/cm^3 and a temperature range 0.086–10 eV. The simulation cell contains 256 Al atoms for temperatures no more than 5 eV and 108 atoms for higher temperatures. The NC11 labels refer to the norm-conserving pseudopotentials with valence electrons being 11. The "corr." term depicts the calculated data obtained by considering the nonlocal pseudopotential correction. Calculation results from Knyazev *et al.* [75,80], Sjostrom *et al.* [21], and Witte *et al.* [22], as well as the experimental results from Milchberg *et al.* [81], Sperling *et al.* [82], and McKelvey *et al.* [83] are shown for comparison. PBE and HSE refer to two different exchange-correlation functionals used in DFT calculations.

[81] for temperatures exceeding 2 eV but exhibit disparities at lower temperatures. In fact, accurately measuring the conductivity of WDM from experiments has always been challenging. For example, the experiment of Milchberg *et al.* did not directly measure the temperature [81] and it was reestimated by Dharma-wardana *et al.* [54] based on the degree of ionization calculated using KSDFT. Similarly, in another first-principles paper by Mo *et al.* [17], the measured temperature from the experiment of Sperling *et al.* is argued to be lower. Additionally, Sperling *et al.* and Milchberg *et al.* conducted ultrafast experiments, where electrons are heated significantly faster than ions. Some studies have suggested that these experiments should be analyzed with a two-temperature model, where the structure of ions should be described with a lower-temperature model [54,55,84,85]. Therefore, we consider the divergence in experimental results may stem from uncertainties in temperature measurement. Besides, since the number of electrons, nonlocal corrections, and frozen-core errors have all converged in our calculations, we suspect the discrepancy between the experimental data and our simulations may come from the lack of considering the nonequilibrium physics, and the exchange-correlation functional may contribute to the discrepancy [22,86].

Figure 3(c) illustrates the thermal conductivities of Al. We compare our calculated results with the experimental data from proton-heated warm dense Al by McKelvey *et al.* [83]. Our results fall within the error bars of the experimental data for Al densities in the range 1.7–2.7 g/cm^3.

Figures 3(b) and 3(d) compare the calculated results with previous first-principles computational papers by Knyazev *et al.* [75], Sjostrom *et al.* [21], and Witte *et al.* [22]. Our results, incorporating the nonlocal potential corrections and utilizing NC11 pseudopotential, are systematically lower than the results obtained from Knyazev *et al.* To explain the differences, we notice that a USPP with three valence electrons without nonlocal potential correction was used for Al in the study of Knyazev *et al.* For comparison, when using the NC3 and NC11 pseudopotential, the electrical and thermal conductivities calculated without nonlocal potential corrections are systematically higher than those with corrections, as respectively shown in Figs. 2(a) and 2(c) for Al density being 2.35 g/cm^3; the conclusion holds when the density increases to 2.7 g/cm^3. Thus, we suspect the discrepancies between our results and those from Knyazev *et al.* may come from the correction term.

Furthermore, both studies of Sjostrom [21] and Witte *et al.* [22] adopted the PAW method, but their results differ, especially at temperatures higher than 2 eV. On the one hand, Sjostrom *et al.* employed the PAW method with three valence electrons for Al, and only the Γ point was used with a cell containing 64 Al atoms. In addition, the electron densities used in KSDFT calculations to yield Kohn-Sham orbitals were obtained from OFDFT calculations without the self-consistent loop, suggesting that the electron densities were approximated. Moreover, to compute the velocity operator, the transversal expression was adopted. Here, the transversal expression means directly substituting $\hat{\mathbf{v}}$ with $-i\hbar\nabla/m_e$ in Eq. (1), considering the PAW method's ability to recover all-electron wavefunctions. Nonetheless, Dajdoš *et al.* [87] pointed out that PAW typically truncates the one-center expansion, leading to inaccurate transversal expression. Consequently, they proposed incorporating a term that describes the dipole moments within the one-center sphere, known as the longitude form [87]. The different results of transversal and longitude forms were also shown by Demyanov and Knyazev's recent paper [88] In contrast, Witte *et al.* employed the PAW method with 11 valence electrons. The cell size and k-point sampling were checked to yield converged

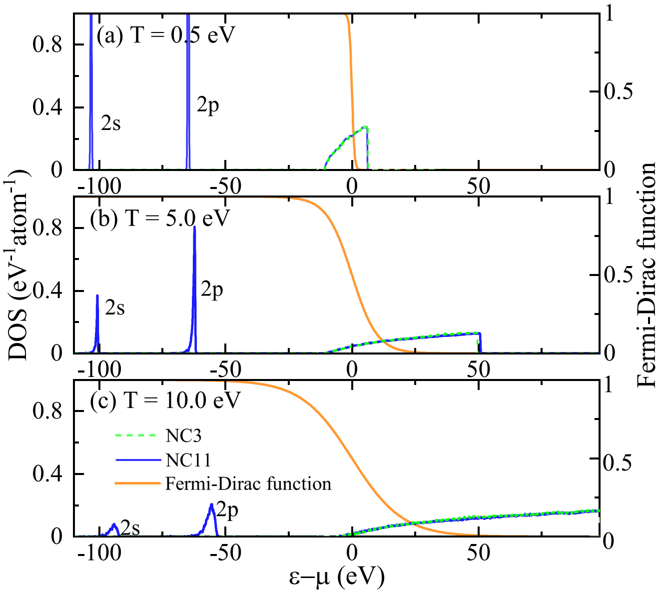

FIG. 4. Density of States (DOS) of warm dense Al at a density of 2.35 g/cm^3 and temperatures of (a) 0.5, (b) 5.0, and (c) 10.0 eV. NC11 and NC3 refer to two norm-conserving pseudopotentials with 11 and 3 valence electrons, respectively. The Fermi-Dirac function is plotted for each temperature.

results. Importantly, they adopted the longitude form [87,89] with corrections. We attribute the discrepancy between the two abovementioned PAW results to the underconvergence of system size, the choice of pseudopotentials, the charge density, and, critically, the consideration of truncation corrections within the PAW framework.

Additionally, Witte *et al.* [22] employed both PBE and HSE (hybrid functional) exchange-correlation functionals. In general, the HSE functional yields smaller electrical conductivity than PBE, but the results from the two functionals converge when the temperature exceeds 4 eV. Comparing with these PBE and HSE data, our results with the nonlocal potential correction and NC11 agree well with the PBE data at 0.2 eV and with the HSE data at higher temperatures. As illustrated in Fig. 3(d), unlike electrical conductivities, both PBE and HSE data from Witte *et al.* [22] lead to similar thermal conductivities, and our results with the nonlocal potential correction and the NC11 pseudopotential match well with these data. In general, despite being based on different methodologies, our NCPP results align well with the PAW results. The agreement indicates the necessity for incorporating additional corrections within the PAW method, as well as accounting for nonlocal potential adjustments in NCPPs, to precisely compute the electrical and thermal conductivities of electrons.

D. Density of states

Figure 4 shows the calculated density of states (DOS) of Al (2.35 g/cm^3) at temperatures of 0.5, 5.0, and 10.0 eV, where μ is the chemical potential. The DOS contributed by $2s$ and $2p$ electrons of Al are labeled. In particular, we plot the DOS of Al by using two NCPPs (NC3 and NC11). In this regard, the $2s$ and $2p$ electrons are absent in the NC3 pseudopotential with three valence electrons but are included in the NC11 pseudopotential with 11 valence electrons. Interestingly, we observe that the $2s$ and $2p$ electrons become more dispersed and shift towards the Fermi energy as temperature increases, and this physical phenomenon can only be captured by DFT calculations with the NC11 pseudopotential.

Additionally, we plot the Fermi-Dirac function for each temperature. We can see that as temperatures increase, the slope of the Fermi-Dirac function becomes smoother. By checking the occupations of these energy states, we find at temperatures of 0.5 and 5 eV, the $2s$ and $2p$ orbitals of Al are fully occupied, and the electrons of the $2p$ orbitals start to ionize at 10 eV. The ionization degree of the $2p$ orbitals is 0.36% at the temperature of 10 eV, as evaluated from the occupation number. This is further confirmed by seeing that the Fermi-Dirac distribution function at 10 eV begins to deviate from 1 at the peak position of the $2p$ orbitals. Meanwhile, the DOS of the scattering states ($3s3p$ and other higher-energy orbitals of Al) around the Fermi level shifts to higher energies as temperature arises, which is captured by both NC3 and NC11 pseudopotentials. In conclusion, even though core electrons are almost nonionized at the temperature of 5 eV, the dispersion and shifting of energy levels for $2s$ and $2p$ electrons affect the computed conductivities, suggesting that a pseudopotential with 11 valence electrons is a more appropriate choice than the NC3 pseudopotential for warm dense Al.

E. Decomposed electrical conductivity

We define a new quantity named decomposed electrical conductivity $\Sigma(\omega,\varepsilon)$ to analyze the contributions of different orbitals to the electrical conductivity. The formula of Σ is

$$\Sigma(\omega,\varepsilon)=\frac{2\pi e^2}{3\omega\Omega}\sum_{ij\alpha\mathbf{k}}W(\mathbf{k})|\langle\Psi_{i\mathbf{k}}|\hat{v}_\alpha|\Psi_{j\mathbf{k}}\rangle|^2 \times[f(\epsilon_{i\mathbf{k}})-f(\epsilon_{j\mathbf{k}})]\delta(\epsilon_{j\mathbf{k}}-\epsilon_{i\mathbf{k}}-\hbar\omega)\delta(\epsilon_{i\mathbf{k}}-\varepsilon), \tag{20}$$

which satisfies the relationship of

$$\sigma(\omega)=\int\Sigma(\omega,\varepsilon)\mathrm{d}\varepsilon. \tag{21}$$

Here $\sigma(\omega)$ is the frequency-dependent electrical conductivity. The results of $\Sigma(\omega,\varepsilon)$ as computed by two different pseudopotentials (NC3 and NC11) with and without the nonlocal potential corrections are displayed in Fig. 5, where μ is the chemical potential. Since conductivities are calculated by extrapolating dynamic conductivities at small frequencies, we choose $\omega = 0.2$ eV as a representative frequency to investigate the effects of pseudopotentials and nonlocal potential corrections. According to the above formulas, the area of each line in Fig. 5 represents the value of $\sigma(\omega)$. As shown in Fig. 2, the consideration of the nonlocal corrections and pseudopotentials with different numbers of electrons results in different behaviors at low and high temperatures. Here, we calculate $\Sigma(\omega,\varepsilon)$ at a temperature of 0.5 eV to represent low temperatures, and at temperatures of 5.0 and 10.0 eV to represent high temperatures. As depicted in Fig. 4, the $2p$

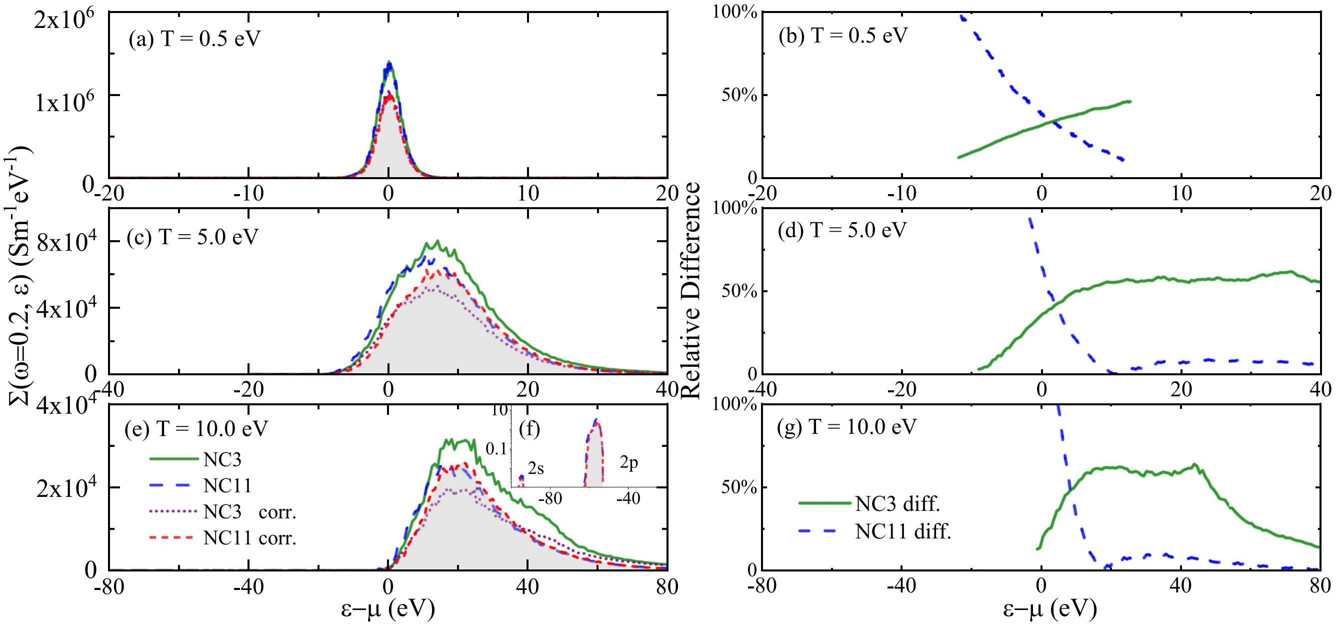

FIG. 5. Decomposed electrical conductivity $\Sigma(\omega, \varepsilon)$ [as defined in Eq. (20)] of warm dense Al with respect to different energies ε at temperatures of (a) 0.5, (c) 5.0, and (d) 10.0 eV. Here μ is the chemical potential. The inset (f) shows the decomposed electrical conductivity contributed by the $2s$ and $2p$ orbitals of Al. Besides, we plot the relative difference of $\Sigma(\omega, \varepsilon)$ between results with and without the nonlocal potential correction for temperatures of (b) 0.5, (d) 5.0, and (g) 10.0 eV. The density of Al is 2.35 g/cm^3 and the frequency ω is chosen to be 0.2 eV. The area under each curve represents the zero-frequency electrical conductivity. NC11 and NC3 refer to two norm-conserving pseudopotentials with 11 and 3 valence electrons, respectively. The term "corr." depicts the nonlocal potential correction. "NCx diff." represents the relative difference computed by the formula of $|\Sigma_{\text{NCx}} - \Sigma_{\text{NCx corr.}}|/\Sigma_{\text{NCx corr.}}$, where x is 3 or 11.

electrons are not ionized at 5.0 eV but begin to ionize at 10.0 eV. We have the following findings.

On the one hand, at the low temperature of 0.5 eV, as shown in Fig. 5(a), we observe that the decomposed electrical conductivity has peaks around the Fermi surface, indicating that only electrons around the Fermi surface ($\varepsilon - \mu = 0$) contribute to the electrical conductivity. This can be understood by the term of $f(\epsilon_{i\mathbf{k}}) - f(\epsilon_{j\mathbf{k}})$ included in the formula of $\Sigma(\omega, \varepsilon)$, and $\partial f(\varepsilon)/\partial\varepsilon$ has the largest value at the peak. We also find the distribution of $\Sigma(\omega, \varepsilon)$ using the NC11 and NC3 pseudopotentials is similar, indicating that the $2s$ and $2p$ electrons in pseudopotentials barely affect the electrical conductivity of Al at 0.5 eV. Meanwhile, the inclusion of nonlocal potential correction significantly reduces the conductivity, highlighting the importance of considering this correction.

Furthermore, Fig. 5(b) illustrates the relative differences between Σ with and without the nonlocal potential correction at 0.5 eV. We observe the relative difference of the NC3 pseudopotential increases with the rise of eigenenergies of electrons, while that of NC11 decreases. This implies the correction becomes more prominent for NC3 than NC11 as shown in Fig. 2(b) because more electrons are excited to high energies with the rise of the temperature.

On the other hand, as the temperature respectively rises to 5 eV and 10 eV in Figs. 5(b) and 5(e), the peaks of Σ shift towards higher energies because the velocity matrix term becomes substantially larger at high-energy bands.

However, the electrical conductivities obtained from the NC3 and NC11 pseudopotentials exhibit substantial discrepancies when the energy $\varepsilon - \mu$ is around the peak of distributions. While the density of states (DOS) of Al calculated by NC3 and NC11 are similar in Fig. 4, the variations in the velocity matrix values calculated with corresponding states, whether with or without nonlocal potential corrections, contribute to these discrepancies. This suggests that the scattering states of the two systems are inherently different. Consequently, even though the $2p$ electrons of Al are either still occupied at 5 eV or barely ionized at 10 eV, the total conductivities show significant differences at these higher temperatures. Figure 5(f) further confirms that the contributions from $2s$ and $2p$ electrons are much smaller compared to the scattering states. These indicate that including the $2s$ and $2p$ orbitals in the NCPP is critical in accurately calculating correct scattering states and predicting the conductivities.

Besides, the relative difference of the NC11 pseudopotential continues to decrease to a small value due to the predominance of the kinetic energy, indicating that the correction becomes less significant with more excited electrons and a shift of peak to higher energies as the temperature rises. In contrast, for the NC3 pseudopotential, the relative differences are in general larger than those from the NC11 pseudopotential, except when $\varepsilon - \mu$ is small.

F. The Lorenz number

The Lorentz number [90,91] characterizes the relationship between the electrical and thermal conductivities and is still not well understood in the warm dense matter region. It is defined as

$$L = \frac{\kappa}{\sigma T}, \tag{22}$$

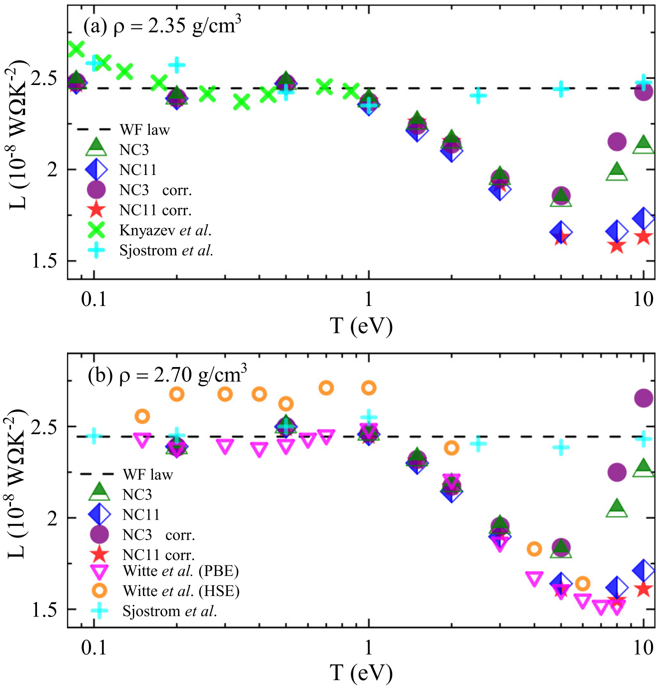

FIG. 6. The Lorenz numbers of warm dense aluminum at a temperature range 0.086–10 eV and densities of (a) 2.35 g/cm^3 and (b) 2.70 g/cm^3. NC11 and NC3 are two norm-conserving pseudopotentials. The label corr. means the nonlocal potential correction is included. The cell contains 256 Al atoms for temperatures no more than 5 eV and 108 atoms for higher temperatures. Besides, first-principles data from Knyazev *et al.* [75], Sjostrom *et al.* [21], and Witte *et al.* [22] are also presented for comparison.

where T is the temperature. Here κ and σ refer to the thermal conductivity and the DC electrical conductivity, respectively. According to the Wiedemann-Franz law [90–92], L is a constant for highly degenerate electrons, approximately equal to 2.445×10^{-8} WΩK^{-2}. According to our calculation results shown in Fig. 6, we have the following findings.

First, at temperatures below 3 eV, the Lorenz number calculated with the NC3 and NC11 pseudopotentials exhibit the same trend. However, as the temperature further increases, the results differ due to the invalidity of the frozen-core approximation used in the NC3 pseudopotential.

Second, the Lorenz number obtained by the NC11 pseudopotential with and without the nonlocal potential corrections are close, indicating that the corrections influence the electrical and thermal conductivities in the same proportion. In contrast, by utilizing the NC3 pseudopotential at the temperature of 8 eV and higher, the nonlocal potential corrections become pronounced.

Third, at temperatures up to 1 eV, the Lorenz number agrees well with the Wiedemann-Franz (WF) law, indicating the inherent relationship between electrical conductivity and thermal conductivity is valid. Meanwhile, the degeneracy parameter, defined as the ratio of temperature to the Fermi temperature T/T_F, is 0.086 at the density of 2.7 g/cm^3 and 0.094 at 2.35 g/cm^3, indicating a high degree of degeneracy in these Al systems.

Fourth, importantly, as the temperature exceeds 1 eV, which falls into the intermediate degenerate range, the Lorenz number starts to decrease and reaches a minimum at the temperature of approximately 8 eV. Specifically, at the density of 2.7g/cm^3, the Lorenz number is 36.7% lower than that predicted by the WF law, while at the density of 2.35 g/cm^3, it is 35.1% lower. The observed trend of the Lorenz number demonstrates that in this region, we cannot calculate thermal conductivity directly from the electrical conductivity using the Wiedemann-Franz law.

Fifth, we compared our results with those of previous studies [21,22,56,75,80]. The results obtained by Recoules *et al.* [56] followed the Wiedemann-Franz law in the temperature range 70–10000 K (0.006–0.862 eV) at a density of 2.35 g/cm^3 (not shown in Fig. 6), agreeing well with our results. The PBE results of Witte *et al.* [22] also match well with our results when using the NC11 pseudopotential with nonlocal potential corrections. However, the HSE results predict a higher Lorenz number. It should be noted that all of these results have taken into account relevant corrections in the velocity matrix. Next, Knyazev *et al.* [75] reported slightly higher values of the Lorenz number at low temperatures. In addition, we also calculate the Lorenz number using σ and κ values from Sjostrom *et al.* [21]. Their results agree well with the Wiedemann-Franz law for all temperatures below 10 eV, yielding unfavorable results as it fails to exhibit a decrease in the Lorenz number at higher temperatures as expected. This may be attributed to the approximations used in their paper, such as the non-self-consistent electronic density obtained by OFDFT.

IV. CONCLUSIONS

Accurate prediction of electron transport coefficients is vital for comprehending warm dense matter. The Kubo-Greenwood formula is extensively employed to calculate the electrical and thermal conductivities of electrons. Nonetheless, the existence of nonlocal terms in the pseudopotentials and the use of the frozen-core approximation in first-principles calculations lead to inaccuracy when the Kubo-Greenwood formula is adopted.

In this paper, we implemented the nonlocal potential corrections with the use of norm-conserving pseudopotentials and plane wave basis under periodic boundary conditions within the ABACUS package. We calculated both electrical and thermal conductivities of liquid Al at 1000 K and warm dense Al within the temperature range 0.2–10 eV. To ensure converged results, we used converged numbers of atoms and k points in our calculation.

We examined the electrical and thermal conductivities of liquid Al at a temperature of 1000 K. By incorporating the nonlocal potential corrections, we obtained results that agreed well with the experimental data. Next, we simulated warm dense Al with temperatures in the range 0.2–10.0 eV at a density of 2.35 g/cm^3. Compared to the results without using the nonlocal potential corrections, we observed lower conductivities when the corrections were applied. Notably, two different norm-conserving pseudopotentials, NC3 and NC11, yielded similar electrical and thermal conductivities at low temperatures. However, as temperatures exceeded 2 eV, discrepancies emerged due to the inadequate frozen core approximation of the 2 s and 2 p electrons of Al. We also simulated Al at a density of 2.70 g/cm^3. The results exhibited similar behaviors to those at 2.35 g/cm^3 and showed reasonable agreement with available experimental data. We also compared our calculated results to those obtained by previous studies.

To gain further insights into the computed conductivities, we analyzed the DOS and the decomposed electrical conductivity at temperatures of 0.5, 5, and 10 eV. We found the core electrons are almost nonionized at the temperature of 5 eV. However, the core electrons affect the high-energy electronic states, resulting in substantially different conductivities as compared to the NC3 pseudopotential. In conclusion, the NC11 pseudopotential provides a more accurate prediction than the NC3 pseudopotential for warm dense Al.

In summary, our findings emphasize the importance of incorporating nonlocal potential corrections when calculating the conductivities of electrons using pseudopotentials. Additionally, the choice of pseudopotential is crucial in accurately determining conductivities, and the frozen-core approximation becomes invalid for calculating conductivities at temperatures before the ionization of corresponding core electrons. However, limited by high computational costs for electrons at extremely high temperatures, traditional KSDFT only allows conductivity calculations for warm dense Al up to a few tens of eV. To overcome this limitation, recent advancements in stochastic DFT [29,30] and mixed stochastic-deterministic DFT [31,32,93] present promising approaches for addressing this challenge.

ACKNOWLEDGMENTS

This work is supported by the National Science Foundation of China under Grants No. 12122401 and No. 12074007. We thank the Electronic Structure Team at AI for Science Institute in Beijing for contributing to the ABACUS package. We thank T. Chen from Peking University for reviewing this manuscript. Part of the numerical simulations was performed on the High-Performance Computing Platform of CAPT.

[1] T. Guillot, Interiors of giant planets inside and outside the solar system, Science **286**, 72 (1999).

[2] F. Wesemael, H. M. Van Horn, M. P. Savedoff *et al.*, Atmospheres for hot, high-gravity stars. I-Pure hydrogen models, Astrophys. J. Suppl. Series **43**, 159 (1980).

[3] J. Lindl, Development of the indirect-drive approach to inertial confinement fusion and the target physics basis for ignition and gain, Phys. Plasmas **2**, 3933 (1995).

[4] M. Bonitz, T. Dornheim, Z. A. Moldabekov, S. Zhang, P. Hamann, H. Kählert, A. Filinov, K. Ramakrishna, and J. Vorberger, *Ab initio* simulation of warm dense matter, Phys. Plasmas **27**, 042710 (2020).

[5] T. G. White, J. Dai, and D. Riley, Dynamic and transient processes in warm dense matter, Phil. Trans. R. Soc. A. **381**, 20220223 (2023).

[6] P. Hohenberg and W. Kohn, Inhomogeneous electron gas, Phys. Rev. **136**, B864 (1964).

[7] W. Kohn and L. J. Sham, Thermal properties of the inhomogeneous electron gas, Phys. Rev. **140**, A1133 (1965).

[8] N. D. Mermin, Thermal properties of the inhomogeneous electron gas, Phys. Rev. **137**, A1441 (1965).

[9] L. H. Thomas, The calculation of atomic fields, Camb. Phil. Soc. **23**, 542 (1927).

[10] E. Fermi, Statistical method to determine some properties of atoms, Rend. Accad. Naz. Lincei. **6**, 602 (1927).

[11] E. L. Pollock and D. M. Ceperley, Simulation of quantum many-body systems by path-integral methods, Phys. Rev. B **30**, 2555 (1984).

[12] D. M. Ceperley and E. L. Pollock, Path-integral computation of the low-temperature properties of liquid ^{4}He, Phys. Rev. Lett. **56**, 351 (1986).

[13] E. W. Brown, B. K. Clark, J. L. DuBois, and D. M. Ceperley, Path-integral Monte Carlo simulation of the warm dense homogeneous electron gas, Phys. Rev. Lett. **110**, 146405 (2013).

[14] S. X. Hu, L. A. Collins, V. N. Goncharov, T. R. Boehly, R. Epstein, R. L. McCrory, and S. Skupsky, First-principles opacity table of warm dense deuterium for inertial-confinement-fusion applications, Phys. Rev. E **90**, 033111 (2014).

[15] K. P. Driver, F. Soubiran, S. Zhang, and B. Militzer, First-principles equation of state and electronic properties of warm dense oxygen, J. Chem. Phys. **143**, 164507 (2015).

[16] Y. H. Ding, A. J. White, S. X. Hu, O. Certik, and L. A. Collins, *Ab initio* studies on the stopping power of warm dense matter with time-dependent orbital-free density functional theory, Phys. Rev. Lett. **121**, 145001 (2018).

[17] C. Mo, Z. Fu, W. Kang, P. Zhang, and X. T. He, First-principles estimation of electronic temperature from x-ray Thomson scattering spectrum of isochorically heated warm dense matter, Phys. Rev. Lett. **120**, 205002 (2018).

[18] C. Mo, Z.-G. Fu, P. Zhang, W. Kang, W. Zhang, and X. T. He, First-principles method for x-ray Thomson scattering including both elastic and inelastic features in warm dense matter, Phys. Rev. B **102**, 195127 (2020).

[19] B. Militzer, F. González-Cataldo, S. Zhang, K. P. Driver, and F. Soubiran, First-principles equation of state database for warm dense matter computation, Phys. Rev. E **103**, 013203 (2021).

[20] V. Vlček, N. de Koker, and G. Steinle-Neumann, Electrical and thermal conductivity of Al liquid at high pressures and temperatures from *ab initio* computations, Phys. Rev. B **85**, 184201 (2012).

[21] T. Sjostrom and J. Daligault, Ionic and electronic transport properties in dense plasmas by orbital-free density functional theory, Phys. Rev. E **92**, 063304 (2015).

[22] B. B. L. Witte, P. Sperling, M. French, V. Recoules, S. H. Glenzer, and R. Redmer, Observations of non-linear plasmon damping in dense plasmas, Phys. Plasmas **25**, 056901 (2018).

[23] Q. Liu, D. Lu, and M. Chen, Structure and dynamics of warm dense aluminum: A molecular dynamics study with density functional theory and deep potential, J. Phys.: Condens. Matter **32**, 144002 (2020).

[24] Q. Liu, J. Li, and M. Chen, Thermal transport by electrons and ions in warm dense aluminum: A combined density functional

theory and deep potential study, Matter Radiat. Extremes **6**, 026902 (2021).

[25] S. Zhang, H. Wang, W. Kang, P. Zhang, and X. T. He, Extended application of Kohn-Sham first-principles molecular dynamics method with plane wave approximation at high energy–From cold materials to hot dense plasmas, Phys. Plasmas **23**, 042707 (2016).

[26] C. Gao, S. Zhang, W. Kang, C. Wang, P. Zhang, and X. T. He, Validity boundary of orbital-free molecular dynamics method corresponding to thermal ionization of shell structure, Phys. Rev. B **94**, 205115 (2016).

[27] A. Blanchet, M. Torrent, and J. Clérouin, Requirements for very high temperature Kohn–Sham DFT simulations and how to bypass them, Phys. Plasmas **27**, 122706 (2020).

[28] X. Liu, X. Zhang, C. Gao, S. Zhang, C. Wang, D. Li, P. Zhang, W. Kang, W. Zhang, and X. T. He, Equations of state of poly-α-methylstyrene and polystyrene: First-principles calculations versus precision measurements, Phys. Rev. B **103**, 174111 (2021).

[29] R. Baer, D. Neuhauser, and E. Rabani, Self-averaging stochastic Kohn-Sham density-functional theory, Phys. Rev. Lett. **111**, 106402 (2013).

[30] Y. Cytter, E. Rabani, D. Neuhauser, and R. Baer, Stochastic density functional theory at finite temperatures, Phys. Rev. B **97**, 115207 (2018).

[31] A. J. White and L. A. Collins, Fast and universal Kohn-Sham density functional theory algorithm for warm dense matter to hot dense plasma, Phys. Rev. Lett. **125**, 055002 (2020).

[32] Q. Liu and M. Chen, Plane-wave-based stochastic-deterministic density functional theory for extended systems, Phys. Rev. B **106**, 125132 (2022).

[33] T. Chen, Q. Liu, Y. Liu, L. Sun, and M. Chen, Combining stochastic density functional theory with deep potential molecular dynamics to study warm dense matter, Matter Radiat. Extremes **9**, 015604 (2024).

[34] V. V. Karasiev, T. Sjostrom, J. Dufty, and S. B. Trickey, Accurate homogeneous electron gas exchange-correlation free energy for local spin-density calculations, Phys. Rev. Lett. **112**, 076403 (2014).

[35] V. V. Karasiev, J. W. Dufty, and S. B. Trickey, Nonempirical semilocal free-energy density functional for matter under extreme conditions, Phys. Rev. Lett. **120**, 076401 (2018).

[36] L. Zhang, J. Han, H. Wang, R. Car, and Weinan E, Deep potential molecular dynamics: A scalable model with the accuracy of quantum mechanics, Phys. Rev. Lett. **120**, 143001 (2018).

[37] L. Zhang, J. Han, H. Wang, W. A. Saidi, R. Car, and Weinan E, End-to-end symmetry preserving inter-atomic potential energy model for finite and extended systems, in *Proceedings of the 32nd International Conference on Neural Information Processing Systems (NIPS'18)*, (Curran Associates Inc., Red Hook, 2018), pp. 4441–4451.

[38] Q. Zeng, X. Yu, Y. Yao, T. Gao, B. Chen, S. Zhang, D. Kang, H. Wang, and J. Dai, *Ab initio* validation on the connection between atomistic and hydrodynamic description to unravel the ion dynamics of warm dense matter, Phys. Rev. Res. **3**, 033116 (2021).

[39] M. Schörner, H. R. Rüter, M. French, and R. Redmer, Extending *ab initio* simulations for the ion-ion structure factor of warm dense aluminum to the hydrodynamic limit using neural network potentials, Phys. Rev. B **105**, 174310 (2022).

[40] M. Schörner, B. B. L. Witte, A. D. Baczewski, A. Cangi, and R. Redmer, *Ab initio* study of shock-compressed copper, Phys. Rev. B **106**, 054304 (2022).

[41] Y. Zhang, C. Gao, Q. Liu, Q. Liu, L. Zhang, H. Wang, and M. Chen, Warm dense matter simulation via electron temperature dependent deep potential molecular dynamics, Phys. Plasmas **27**, 122704 (2020).

[42] D. R. Hamann, M. Schlüter, and C. Chiang, Norm-conserving pseudopotentials, Phys. Rev. Lett. **43**, 1494 (1979).

[43] L. Kleinman and D. M. Bylander, Efficacious form for model pseudopotentials, Phys. Rev. Lett. **48**, 1425 (1982).

[44] D. R. Hamann, Optimized norm-conserving Vanderbilt pseudopotentials, Phys. Rev. B **88**, 085117 (2013).

[45] D. R. Hamann, Erratum: Optimized norm-conserving Vanderbilt pseudopotentials [Phys. Rev. B 88, 085117 (2013)], Phys. Rev. B **95**, 239906(E) (2017).

[46] M. Schlipf and F. Gygi, Optimization algorithm for the generation of ONCV pseudopotentials, Comput. Phys. Commun. **196**, 36 (2015).

[47] M. van Setten, M. Giantomassi, E. Bousquet, M. Verstraete, D. Hamann, X. Gonze, and G.-M. Rignanese, The pseudodojo: Training and grading a 85 element optimized norm-conserving pseudopotential table, Comput. Phys. Commun. **226**, 39 (2018).

[48] D. Vanderbilt, Soft self-consistent pseudopotentials in a generalized eigenvalue formalism, Phys. Rev. B **41**, 7892 (1990).

[49] P. E. Blöchl, Projector augmented-wave method, Phys. Rev. B **50**, 17953 (1994).

[50] S. Baroni, S. de Gironcoli, A. Dal Corso, and P. Giannozzi, Phonons and related crystal properties from density-functional perturbation theory, Rev. Mod. Phys. **73**, 515 (2001).

[51] D. S. Ivanov and L. V. Zhigilei, Combined atomistic-continuum modeling of short-pulse laser melting and disintegration of metal films, Phys. Rev. B **68**, 064114 (2003).

[52] M. M. Marinak, S. W. Haan, T. R. Dittrich *et al.*, A comparison of three-dimensional multimode hydrodynamic instability growth on various National Ignition Facility capsule designs with HYDRA simulations, Phys. Plasmas **5**, 1125 (1998).

[53] V. N. Korobenko and A. D. Rakhel, Observation of a first-order metal-to-nonmetal phase transition in fluid iron, Phys. Rev. B **85**, 014208 (2012).

[54] M. Dharma-wardana and F. Perrot, Resistivity and dynamic conductivity of laser-pulse heated aluminum up to 10^6 K and along the shock Hugoniot up to 20 Mbars, Phys. Lett. A **163**, 223 (1992).

[55] M. W. C. Dharma-wardana, Dynamic conductivity and plasmon profile of aluminum in the ultra-fast-matter regime, Phys. Rev. E **93**, 063205 (2016).

[56] V. Recoules and J.-P. Crocombette, *Ab initio* determination of electrical and thermal conductivity of liquid aluminum, Phys. Rev. B **72**, 104202 (2005).

[57] Y. Laudernet, J. Clérouin, and S. Mazevet, *Ab initio* simulations of the electrical and optical properties of shock-compressed SiO_2, Phys. Rev. B **70**, 165108 (2004).

[58] F. Lambert and V. Recoules, Plastic ablator and hydrodynamic instabilities: A first-principles set of microscopic coefficients, Phys. Rev. E **86**, 026405 (2012).

[59] M. M. G. Alemany, L. J. Gallego, and D. J. González, Kohn-Sham *ab initio* molecular dynamics study of liquid Al near melting, Phys. Rev. B **70**, 134206 (2004).

[60] D. Kang, S. Zhang, Y. Hou, C. Gao, C. Meng, J. Zeng, and J. Yuan, Thermally driven Fermi glass states in warm dense matter: Effects on terahertz and direct-current conductivities, Phys. Plasmas **26**, 092701 (2019).

[61] M. Chen, G.-C. Guo, and L. He, Systematically improvable optimized atomic basis sets for *ab initio* calculations, J. Phys.: Condens. Matter **22**, 445501 (2010).

[62] P. Li, X. Liu, M. Chen, P. Lin, X. Ren, L. Lin, C. Yang, and L. He, Large-scale *ab initio* simulations based on systematically improvable atomic basis, Comput. Mater. Sci. **112**, 503 (2016).

[63] See Supplemental Material at http://link.aps.org/supplemental/10.1103/PhysRevB.110.014207 for fitting methods and results; convergence about the number of atomic configurations; conductivity results using temperature dependent XC; conductivity data of all methods to plot Figs. 2 and 3, which includes Ref. [94].

[64] A. F. Starace, Length and velocity formulas in approximate oscillator-strength calculations, Phys. Rev. A **3**, 1242 (1971).

[65] A. J. Read and R. J. Needs, Calculation of optical matrix elements with nonlocal pseudopotentials, Phys. Rev. B **44**, 13071 (1991).

[66] H. J. Monkhorst and J. D. Pack, Special points for Brillouin-zone integrations, Phys. Rev. B **13**, 5188 (1976).

[67] M. S. Hybertsen and S. G. Louie, *Ab initio* static dielectric matrices from the density-functional approach. I. Formulation and application to semiconductors and insulators, Phys. Rev. B **35**, 5585 (1987).

[68] L.-W. Wang and M. P. Teter, Kinetic-energy functional of the electron density, Phys. Rev. B **45**, 13196 (1992).

[69] S. Nosé, A unified formulation of the constant temperature molecular dynamics methods, J. Chem. Phys. **81**, 511 (1984).

[70] W. G. Hoover, Canonical dynamics: Equilibrium phase-space distributions, Phys. Rev. A **31**, 1695 (1985).

[71] A. Dal Corso, Pseudopotentials periodic table: From H to Pu, Comput. Mater. Sci. **95**, 337 (2014).

[72] N. Troullier and J. L. Martins, Efficient pseudopotentials for plane-wave calculations, Phys. Rev. B **43**, 1993 (1991).

[73] J. P. Perdew, K. Burke, and M. Ernzerhof, Generalized gradient approximation made simple, Phys. Rev. Lett. **77**, 3865 (1996).

[74] http://abacus.ustc.edu.cn/main.htm.

[75] D. Knyazev and P. Levashov, *Ab initio* calculation of transport and optical properties of aluminum: Influence of simulation parameters, Comput. Mater. Sci. **79**, 817 (2013).

[76] K. C. Mills, B. J. Monaghan, and B. J. Keene, Thermal conductivities of molten metals: Part 1. Pure metals, Int. Mater. Rev. **41**, 209 (1996).

[77] W.-K. Rhim and T. Ishikawa, Noncontact electrical resistivity measurement technique for molten metals, Rev. Sci. Instrum. **69**, 3628 (1998).

[78] A. B. Abdellah, J. G. Gasser, and B. Grosdidier, Resistivity and thermoelectric power of molten aluminium: Experiment and theory, Philos. Mag. **85**, 1949 (2005).

[79] R. Brandt and G. Neuer, Electrical resistivity and thermal conductivity of pure aluminum and aluminum alloys up to and above the melting temperature, Int. J. Thermophys. **28**, 1429 (2007).

[80] D. V. Knyazev and P. R. Levashov, Transport and optical properties of warm dense aluminum in the two-temperature regime: *Ab initio* calculation and semiempirical approximation, Phys. Plasmas **21**, 073302 (2014).

[81] H. M. Milchberg, R. R. Freeman, S. C. Davey, and R. M. More, Resistivity of a simple metal from room temperature to 10^6 k, Phys. Rev. Lett. **61**, 2364 (1988).

[82] P. Sperling, E. J. Gamboa, H. J. Lee, H. K. Chung, E. Galtier, Y. Omarbakiyeva, H. Reinholz, G. Röpke, U. Zastrau, J. Hastings, L. B. Fletcher, and S. H. Glenzer, Free-electron X-ray laser measurements of collisional-damped plasmons in isochorically heated warm dense matter, Phys. Rev. Lett. **115**, 115001 (2015).

[83] A. McKelvey, G. Kemp, P. Sterne *et al.*, Thermal conductivity measurements of proton-heated warm dense aluminum, Sci. Rep. **7**, 7015 (2017).

[84] N. Wetta and J.-C. Pain, Consistent approach for electrical resistivity within Ziman's theory from solid state to hot dense plasma: Application to aluminum, Phys. Rev. E **102**, 053209 (2020).

[85] N. Wetta and J.-C. Pain, Issues in the calculations of dc conductivity of warm dense aluminium, Contrib. Plasma Phys. **62**, e202200003 (2022).

[86] B. B. L. Witte, L. B. Fletcher, E. Galtier, E. Gamboa, H. J. Lee, U. Zastrau, R. Redmer, S. H. Glenzer, and P. Sperling, Warm dense matter demonstrating non-drude conductivity from observations of nonlinear plasmon damping, Phys. Rev. Lett. **118**, 225001 (2017).

[87] M. Gajdoš, K. Hummer, G. Kresse, J. Furthmüller, and F. Bechstedt, Linear optical properties in the projector-augmented wave methodology, Phys. Rev. B **73**, 045112 (2006).

[88] G. S. Demyanov, D. V. Knyazev, and P. R. Levashov, Continuous Kubo-greenwood formula: Theory and numerical implementation, Phys. Rev. E **105**, 035307 (2022).

[89] M. French and R. Redmer, Electronic transport in partially ionized water plasmas, Phys. Plasmas **24**, 092306 (2017).

[90] R. Franz and G. Wiedemann, Ueber die wärmeleitungsfähigkeit der metalle, Ann. Phys. (Leipzig) **165**, 497 (1853).

[91] L. Lorenz, Bestimmung der wärmegrade in absolutem maasse, Ann. Phys. (Leipzig) **223**, 429 (1872).

[92] J. Ziman, *Electrons and Phonons: The Theory of Transport Phenomena in Solids* (Oxford University Press, Oxford, 2001).

[93] A. J. White, L. A. Collins, K. Nichols, and S. X. Hu, Mixed stochastic-deterministic time-dependent density functional theory: Application to stopping power of warm dense carbon, J. Phys.: Condens. Matter **34**, 174001 (2022).

[94] M. P. Desjarlais, J. D. Kress, and L. A. Collins, Electrical conductivity for warm, dense aluminum plasmas and liquids, Phys. Rev. E **66**, 025401(R) (2002).